AIAA JOURNAL
Vol. 58, No. 8, August 2020

Droplet Deformation and Trajectory Without Interferences in the Incoming Airfoil Shoulder Region

Adelaida Garcia-Magariño* and Suthyvann Sor†
National Institute of Aerospace Technology, 28850 Madrid, Spain
and
Angel Velazquez‡
Technical University of Madrid, 28040 Madrid, Spain

https://doi.org/10.2514/1.J058792

A new experimental campaign has been conducted in the shoulder region of an incoming airfoil of chord 1050 mm, where droplets are separated enough to neglect interferences between them. Droplets of three sizes (500, 950, and 1250 μm of radius) were allowed to fall in the path of an incoming airfoil while shadowgraph images were recorded by a high-speed video camera at 40,000 fps. The airfoil model was placed at the end of a rotating arm and moved at four velocities (30, 40, 50, and 60 m/s). Three different regions of the shoulder were tested. Droplet deformation and trajectories are presented. Droplets evolve as a conjunction of two half-oblate spheroids that tilt as the model approaches. The tilting is larger in the higher regions of the shoulder. The trajectory model derived for droplet in the stagnation line of a moving airfoil has been formally derived for the shoulder region and applied to the experimental data, showing very good agreement being the mean discrepancy less than 4% for the trajectory and 10% for the deformation.

Nomenclature

A_d	=	droplet surface area
C_D	=	drag coefficient
$D_{\max}$	=	droplet maximum diameter
$D_{\min}$	=	droplet minimum diameter
d	=	horizontal distance to the stagnation point of the airfoil
g	=	gravity acceleration
k	=	trajectory model constant, which is equal to 9
R_d	=	droplet initial radius
Re	=	Reynolds number
T	=	time
U_m	=	airfoil model velocity
V_{air_x}	=	horizontal coordinate of the air velocity
V_{air_y}	=	vertical coordinate of the air velocity
V_s	=	slip velocity between the droplet and the air
X_{PIV}	=	horizontal coordinate in airfoil frame of reference
x	=	horizontal droplet position
x_{airfoil}	=	airfoil model horizontal coordinate
Y_{PIV}	=	span-direction coordinate in airfoil frame of reference
y	=	vertical droplet position
y_{airfoil}	=	airfoil model vertical coordinate
Z_{PIV}	=	vertical coordinate in airfoil frame of reference
μ_{air}	=	air viscosity
μ_d	=	droplet viscosity
ρ_{air}	=	air density
ρ_d	=	droplet density

Presented as Paper 2019-3306 at the AIAA Aviation 2019 Forum, Dallas, TX, June 16–21, 2019; received 9 October 2019; revision received 20 February 2020; accepted for publication 7 April 2020; published online 18 May 2020.

*Experimental Aerodynamics, Carretera de Ajalvir Km 4, Torrejón de Ardoz; garciamga@inta.es.

†Experimental Aerodynamics, Carretera de Ajalvir Km 4, Torrejón de Ardoz; sors@inta.es.

‡Professor of Aerospace Engineering, Fluid Mechanics and Aerospace Propulsion Department, Plaza Cardenal Cisneros 3; angel.velazquez@upm.es.

I. Introduction

THE problem concerning water droplet impinging on airfoils is of vital importance in areas such as ice accretions on wing surfaces, especially with supercooled large droplet (SLD) [1,2]. A collision of a supercooled water droplet on an object creates ice on its surface. Different models of ice accretion due to the impact of supercooled droplets in aircraft can be found in the works of Honsek et al. [3], Iuliano et al. [4], Blake et al. [5], Wang et al. [6], and Trontin and Villedieu [7]. The problem of in-flight icing is that it can cause significantly changes in the flight performance, stability, and control that, in the end, can result in aircraft failure [8]. Some reviews on this can be found in the works of Baars et al. [9] and Caliskan and Hajiyev [10]. The first stage in any icing analysis is to calculate what is known as the water collection or catch-efficiency distribution, which determines where and at what rate the cloud water droplets are deposited on the surface of the body under investigation. Because of the forward velocity of the aircraft, supercooled droplets impinge on the surface of the aircraft when the aircraft flies through a supercooled cloud [11,12]. The trajectory that a droplet follows, and therefore the location at which it will impact the surface, depends mostly on the droplet drag, as the trajectory is determined mostly by the drag force on the droplet [13], which in turn depends on its shape and size [1]. The ratio of the inertia to the aerodynamic forces determines whether a droplet impacts the surface or is swept past the body in the airflow. Larger droplets tend to deviate more from the streamlines having less curved trajectories, and then impinging on the airfoil [13].

Several investigations have been dedicated to droplet deformation due to crossflows; however, most of them assumed a constant airstream. This is the case of the works of Aalburg et al. [14] and Mashayek and Ashgriz [15], who addressed the problem numerically. Aalburg et al. [14] studied the deformation, drag, and breakup properties of round drops subjected to shock-wave disturbances, whereas Mashayek and Ashgriz [15] developed an analytical–numerical model to calculate the deformation and spreading of axisymmetric and two-dimensional liquid drops in a gas stream based on an approximate series solution of the Navier–Stokes and assuming a quasi-static flow. However, the most known modelization of droplet deformation is the Taylor analogy breakup model (O'Rourke and Amsden [16]), which establishes an analogy between the droplet and a mass-string system. From an experimental point of view, there are a large number of experiments in facilities, such as shock tubes and wind tunnels. This is the case, for example, of the work of Wierzba [17], who conducted experiments in a horizontal wind tunnel where a stream of uniform water droplets was allowed to fall perpendicularly

to the continuous stream of air. However, the actual flowfield encountered by the droplets in the vicinity of airfoils is a continuously accelerated flowfield instead of the constant airstream found in facilities, such as shock tubes and wind tunnels.

Alesekyenko et al. [18] published a paper dedicated to study the interaction of SLD with an icing airfoil surface, and in the paper of Shimura and Yamamoto [19], the effect of droplet deformation models on SLD icing was investigated by means of simulation. The model of the drag coefficient was confirmed to influence the ice shape, the droplet impinging limit, and the icing limit. The need of an investigation of the unsteady effect of the droplet drag coefficient, including the droplet deformation and internal circulation for modeling purpose, is well presented by Shao et al. [20] and Qu et al. [21], who addressed the issue numerically. A recent study of the droplet internal flow under shock impact has been performed numerically and theoretically by Guan et al. [22]. On the one hand, Shao et al. [20] studied the unsteady drag coefficient of liquid droplets in the context of liquid atomization. Therefore, the droplet acceleration considered is one of those immersed in a continuous air jet: decelerating relative flow. They concluded that the unsteady drag coefficient was always larger than the steady standard drag coefficient for the decelerating relative flow. On the other hand, Qu et al. [21] elucidated the difference between accelerating and decelerating drops, obtaining that the drag coefficient of a decelerated drop is always larger than that of an accelerated flow. Another interesting recent work is the one of Meng and Colonius [23]. They also concluded that the droplet deformation alters its drag properties, and unsteady effects become dominant.

Unsteadiness should be even more important when, instead of a constant high airstream, droplets are subjected to a continuously accelerating airstream, such as in the vicinity of the leading edge of an airfoil. For these conditions, little information is available in the literature. The first approach to this situation is the work of Vargas and Feo [24]. Vargas and Feo [24], in an Instituto Nacional de Técnica Aeroespacial (INTA)/NASA collaboration, published an experimental study, in which a rotating arm facility with an airfoil placed at the end of an arm and equipped with a high-speed imaging system was used to gather information on a series of water-droplet global parameters as they intersected the airfoil path. Although water droplets were at ambient temperature, this experiment, which involved extensive visualization, could be considered as the first approach providing experimental insight into the phenomenon. However, it only covers droplet diameters up to 500 μm and one airfoil chord. Further studies were needed in this field, including different airfoil sizes and droplet sizes of up to 3 mm in diameter to study the size range of the SLD encountered [25]. As a continuation, further experiments were conducted by Vargas et al. in 2011 [25] and 2012 [26] in the rotating arm facility at INTA for water-droplet diameter ranging from 500 to 1800 μm; model velocities from 50 to 90 m/s; and for three model chord sizes of 0.21, 0.47, and 0.71 m. From the analysis of those experiments, a set of investigations were conducted [27–31]. First, in the work of Garcia-Magariño et al. [27], the deformation and breakup of four droplet diameters (0.354, 0.580, 0.782, and 1056 mm) were presented and studied. They concluded that the transient effects (associated to the fact that the slip velocity past the droplets continuously increased) proved to play a relevant role. At the same time, Sor and Garcia-Magariño and Sor et al. [28,29] developed a droplet deformation and trajectory model for droplets in the stagnation line of a moving airfoil that proved to be considerably more accurate than previous models. Although all these studies [27–31] were based on experiments, where droplets were at ambient temperature, Veras-Alba et al. [32] conducted new experiments with supercooled droplets and compared the results with droplets at ambient temperature. They concluded that the fact that droplets are supercooled does not change the deformation process. Therefore, experiments at ambient temperature are still relevant in the context of SLD.

All previous models for droplet deformation and trajectory in the vicinity of the leading edge of an airfoil were developed in the stagnation line of a moving airfoil. However, in the context of SLD ice accretion, the most interesting region where these models should be applied is the shoulder region of the airfoil. In this region, the droplet or the resultant droplets of a possible breakup may impinge or surpass the model, thus modifying the amount and location of droplets that reach the model. The only results found in the literature of droplet deformation and breakup in the shoulder region of an airfoil were the one from Sor et al. [33]. Sor et al. [33] conducted experiments for only one droplet size (1 mm) and one airfoil chord (0.47 m), at three different heights from the stagnation line. The droplet trajectories were compared with those obtained by the theoretical model of Sor et al. [29] for the stagnation line, and some discrepancies were obtained. The images obtained for deformation showed that there may be some interferences between droplets that could be responsible for the discrepancies found, and they concluded that new experiments should be conducted with droplets with more distance between droplets so that the interferences could be neglected.

As a continuation of the previous work, in the present investigation, new experiments have been conducted in the shoulder, where the distance between droplets has been increased. Three droplet sizes at three different heights from the stagnation line for a bigger airfoil model have been tested. The aim of the study was to present the results of new experiments on droplet deformation in the shoulder region without interferences between droplets, and to elucidate whether the discrepancies found in Sor et al. [33] were due indeed to the interferences between droplets. Additionally, the model of Sor et al. [29] was formally derived for the stagnation line of an airfoil. Therefore, a formal derivation for the shoulder region of an airfoil will also be presented. Experimental data will provide information of the validity of the model for the shoulder region, which is interesting in the context of SLD ice accretion modeling. In particular, this model could be used in the prediction of the droplet breakup according to the breakup criterion by Garcia-Magariño et al. [34], which needs to know the slip velocity and its variation with time.

II. Experimental Setup

New experiments have been conducted in the shoulder region of an airfoil. The experimental setup consisted of four modules: the rotating arm unit, the airfoil attached at the end of the arm, the monosized droplet generator, and the high-speed imaging system. Figure 1 shows the experimental setup components before a run. A stream of droplets are generated by a monosized droplet generator and allowed to fall in the path of an incoming airfoil. The airfoil model is attached at the end of the rotating arm at controlled velocities. A high-speed video camera recorded images of the droplets while they were intercepted by the airfoil by illuminating them from behind, using the known technique of shadowgraph.

A. Rotating Arm Unit

The rotating arm unit consisted of an arm of 2.18 m moved by a 5 kW motor with a gear box reduction that allowed velocities up to 70 m/s at the end of the arm. The motor is mounted on a support structure that rests on a solid base attached to the floor through four slip ring vibration dampers (see Fig. 2). The motor is placed inside a support structure with the axle vertical in the direction of the ceiling. A gear box reduction reduces the motor revolution speed for an improved use of the motor energy. The rotating arm is attached to the axle of the motor and it has a length of 2.18 m. The revolutions per minute of the arm are measured using a light-emitting diode (LED) optical system, and they are controlled from the control room, which is separated from the rotating rig by a safety glass window and a steel safety mesh (see Fig. 2).

B. Airfoil Model

The airfoil model used has the same geometry as the one used in previous experiments [25–29], but different chord size, which is now 1050 mm. The model consists of a central two-dimensional airfoil body, whose coordinates are shown in Table 1, and two lateral parts, which are half-revolution bodies having the same profile. The span of the central body is 300 mm. Actual views of the airfoil model are shown in Figs. 3a–3d. The type of airfoil used has a blunt shape that

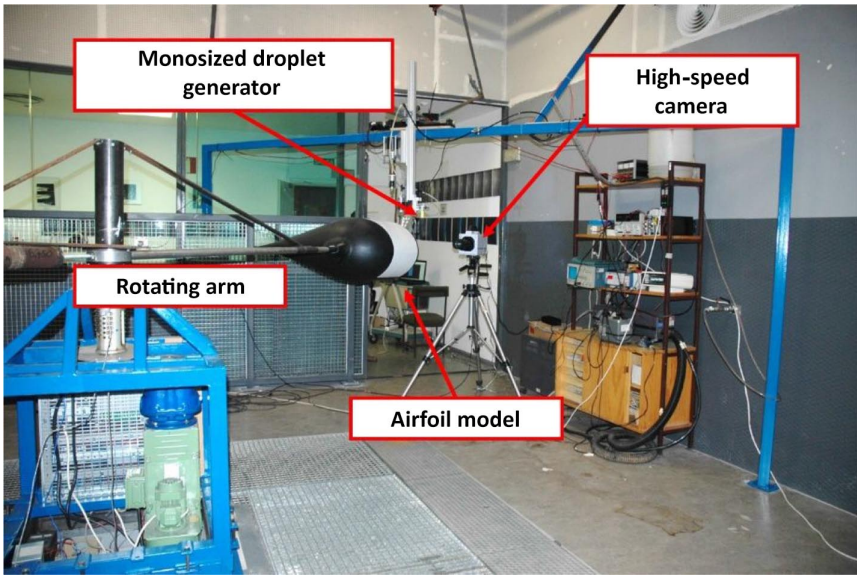

Fig. 1 Experimental setup components in the test cell before a run.

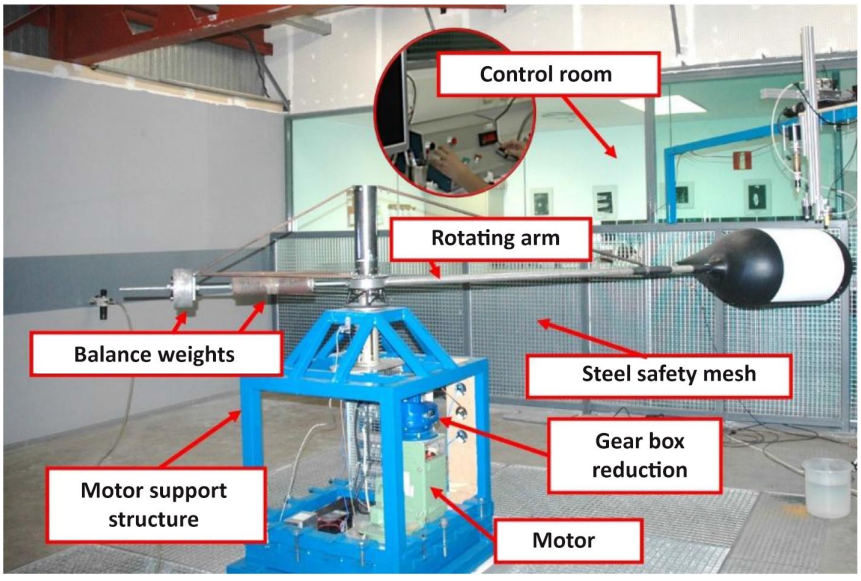

Fig. 2 Experimental setup components in the test cell before a run.

Table 1 Airfoil model coordinates

$x_{airfoil}$, mm	$y_{airfoil}$, mm	$x_{airfoil}$, mm	$y_{airfoil}$, mm	$x_{airfoil}$, mm	$y_{airfoil}$, mm
1050.00	0.00	787.50	66.47	262.50	210.75
1048.88	0.90	757.20	75.75	233.32	208.46
1045.51	1.49	725.91	85.54	205.40	204.04
1039.91	2.66	693.76	96.03	178.85	197.39
1033.16	4.41	660.88	107.04	153.77	188.69
1022.14	6.70	627.43	118.46	130.28	178.45
1010.04	9.39	593.51	130.20	108.49	166.36
995.86	12.61	559.34	142.05	88.48	153.13
979.66	16.23	525.00	153.96	70.34	138.18
961.52	20.45	490.67	165.56	54.14	122.84
941.51	25.20	456.48	176.72	39.96	105.76
919.72	30.58	422.57	186.87	27.86	88.38
896.23	36.48	389.12	196.35	17.89	70.73
871.15	43.07	356.24	203.52	10.09	52.26
844.60	50.26	324.09	208.45	1.34	32.50
816.68	58.13	292.79	210.67	1.12	14.56

simulates a scaled version of the type of leading edge found on large transport airfoils.

The rigidity of the arm where the model is mounted would not allow the use of a model that would generate lift. Therefore, a symmetric model was used with 0 pitching angle due to the limitations of the rotating rig facility. In a more generic in-flight situation, the model would have a pitching angle and would not be symmetric. However, for the purpose of this study, the important issue to be addressed is the validity of the Sor et al.'s model [29] in the shoulder region of the model. The main difference between the stagnation region and the shoulder region is the variation of the slip velocity direction. This is addressed by performing experiments in different regions at three heights above the stagnation line of the model. These three regions were chosen to change as much as possible the slip velocity direction.

Previous experiments were conducted in a scaled model mounted in the rotating rig facility to measure the flowfield velocity using a TSI particle image velocimetry (PIV) system. The detailed description of

these experiments can be found in Ref. [27]. However, for the sake of completeness, a brief description is shown here. Flow illumination was provided by a pulsed Nd:YAG 190 mJ laser, whose pulses lasted for 8 ns. A PowerView Plus 4 MP camera was used to obtain images with a resolution of 2048 × 2048 pixels. The camera lenses were AF-S VR Micro-Nikkor 105 mm f/2.8 G IF-ED Nano Crystal Coat, AF Nikkor 80–200 mm f/2.8 D IF-ED, and Nikkor 50 mm f/1.4. The flow was seeded with oil particles of 1 μm (small enough to follow the flow). Both a vertical plane (the one tangent to the airfoil trajectory that intersects the droplet generator) and a horizontal plane (intersecting the airfoil leading edge) were illuminated. The combination of a trigger and a synchronizer allowed for taking PIV images at the fixed interrogation windows (where droplets fall) for any position of the model airfoil during its circular trajectory. In the end, two average velocity maps over at least 50 images were obtained for the vertical and horizontal planes in the airfoil frame of reference. Those maps can be seen in Figs. 3e–3h. It can be observed that there is a region in the center of the leading edge up to 10% of the chord (100 mm) in the spanwise direction, where the air velocity in this spanwise direction is less than 10% of the model velocity.

C. Monosized Droplet Generator

A custom-made droplet generator was fabricated at INTA to obtain a stream of droplets, where droplets are enough separated to neglect the interferences between them (see Fig. 4). This droplet generator operates on the same principle as other monosized droplet generators: vibrating a laminar water jet at a selected frequency to generate the droplets of the desired size. A function generator provides a signal at the desired frequency that is then amplified up to 30 V and connected to a piezoelectric membrane that is inside the droplet generator. The water is supplied inside the droplet generator by a pump, and then falls passing through a calibrated orifice generating a jet of a specific diameter. The vibration of the piezoelectric makes the jet vibrates, and by this vibration, a stream of droplets is generated. An example of the stream of droplets of the three sizes used in these experiments is shown in Fig. 4 (right).

D. High-Speed Imaging System

The high-speed imaging system consisted of a high-speed video camera and a light power source that illuminates the droplets

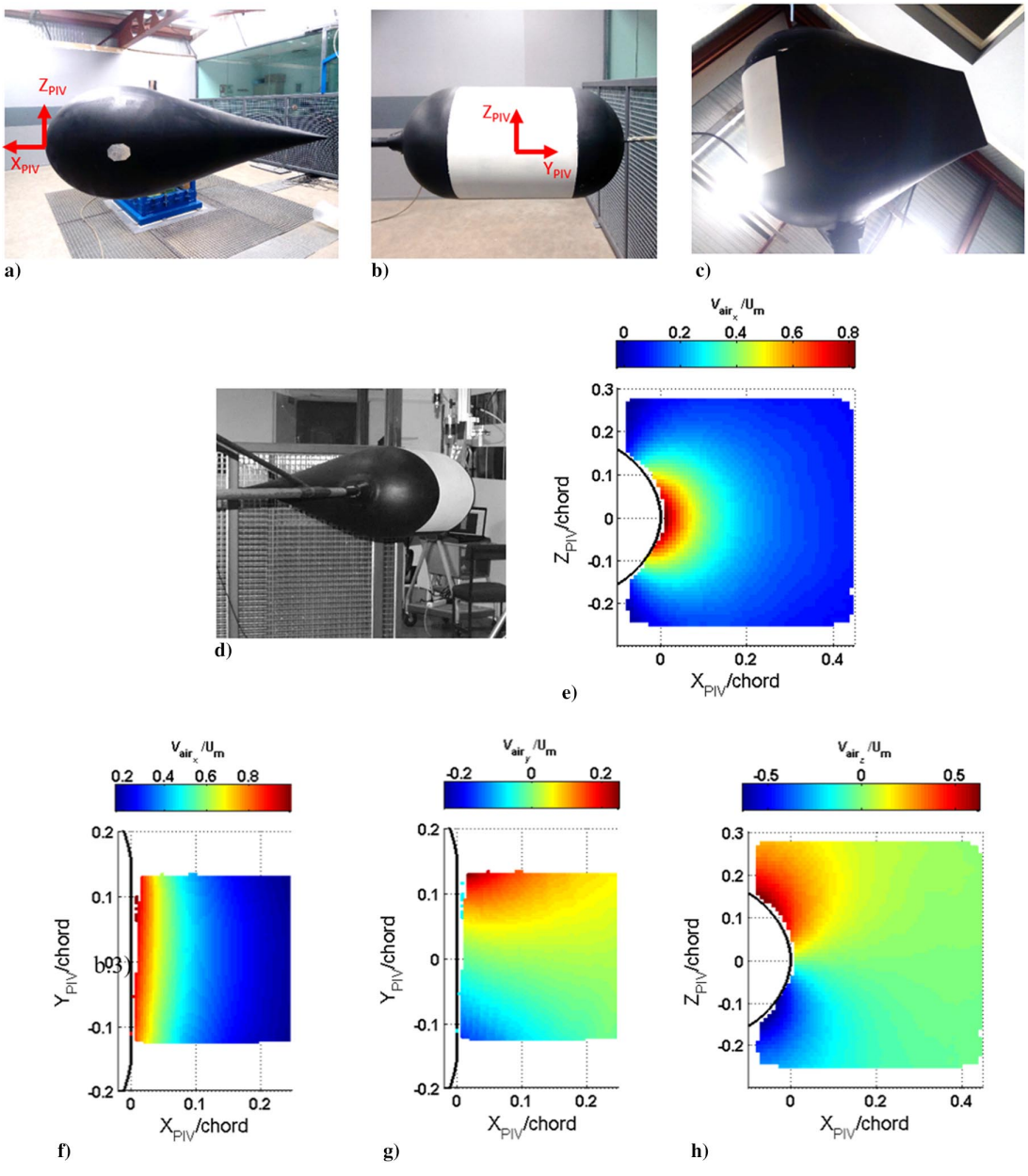

Fig. 3 a–d) Airfoil model views and e–h) PIV velocity maps.

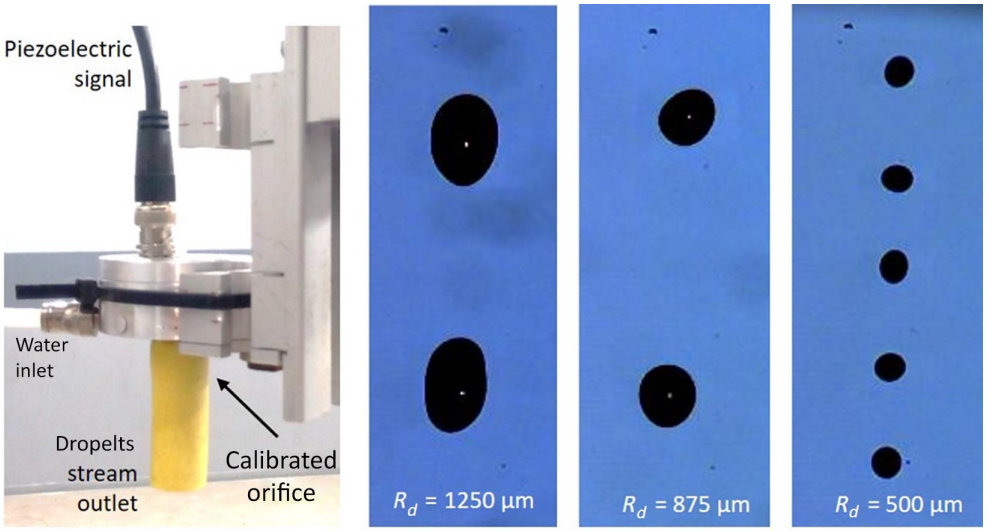

Fig. 4 Monosized droplet generator (left) and images of the droplets generated (right).

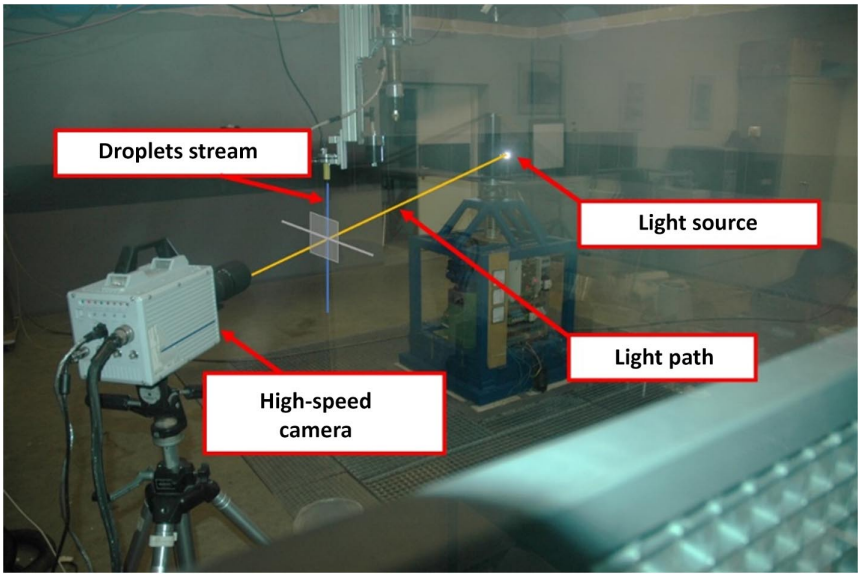

Fig. 5 Experimental setup of the high-speed recording system.

from behind (see Fig. 5). The high-speed camera was the Photron Fastcam SA4 camera and the lens used was the AF Micro-Nikkor 200 mm f/4D IF-ED. The power source was a zoomable 3 W LED, and it was mounted on a tripod to orientate the light path perpendicular to the charge-coupled device of the camera. The magnification of the images was 20 pixels/mm, and the resolution of each image was 192×336 pixels. The acquisition rate was 40,000 fps. A previous study based on high-order singular value decomposition [35] led to the conclusion that tests could be done at a lower acquisition rate than previous studies in the rotating arm (75,000 fps) for deformation studies. The shutter was 1/98,000 s.

III. Experimental Test Matrix and Data Analysis

A. Test Matrix

Thirty-six cases were addressed experimentally corresponding to the variation of the following three parameters:

1) Parameter 1 (field of view [FOV]): Three different FOV were addressed corresponding to three different regions of the shoulder. The heights of the midline of the FOV with respect to the stagnation line of the airfoil were, respectively, 50, 90, and 130 mm. These three regions were chosen to variate as much as possible the slip velocity direction.

2) Parameter 2 (U_m): Four different approaching airfoil velocities (U_m) were tested, which were 30, 40, 50, and 60 m/s.

3) Parameter 3 (R_d): Three different droplet sizes were tested corresponding to initial droplet radii R_d of 500, 950, and 1250 μm. The droplet radii were chosen to cover the maximum droplet radius value expected in aircraft icing environments with SLDs, which is 1115 μm according to table 2 in Ref. [36].

The airfoil size remained unchanged during the tests, being its chord length of 1050 mm. For each experimental case, three droplets were analyzed to ensure repeatability. Table 2 shows the case key for each case.

The Reynolds number and the Weber number, defined using the model velocity as the characteristic velocity and the droplet diameter as the characteristic length, for each case can be observed in Tables 3 and 4, respectively.

Figure 6 shows the regions covered by each FOV. For each FOV and for each airfoil model velocity, the air flowfield generated would be different. Figure 7 shows the air velocity modulus that the droplet would encounter as a function of the distance of the stagnation point in the leading edge of the airfoil (d), for each FOV and for each model

Table 2 Case key for each experimental case

	$R_d = 1250\ \mu$m			$R_d = 950\ \mu$m			$R_d = 500\ \mu$m		
U_m, m/s	FOV 1	FOV 2	FOV 3	FOV 1	FOV 2	FOV 3	FOV 1	FOV 2	FOV 3
30	1	2	3	4	5	6	7	8	9
40	10	11	12	13	14	15	16	17	18
50	19	20	21	22	23	24	25	26	27
60	28	29	30	31	32	33	34	35	36

Table 3 Reference Reynolds number for each experimental case

	$R_d = 1250\ \mu$m			$R_d = 950\ \mu$m			$R_d = 500\ \mu$m		
U_m, m/s	FOV 1	FOV 2	FOV 3	FOV 1	FOV 2	FOV 3	FOV 1	FOV 2	FOV 3
30	6,800	6,800	6,800	5,100	5,100	5,100	2,700	2,700	2,700
40	9,000	9,000	9,000	6,900	6,900	6,900	3,600	3,600	3,600
50	11,300	11,300	11,300	8,600	8,600	8,600	4,500	4,500	4,500
60	13,500	13,500	13,500	10,300	10,300	10,300	5,400	5,400	5,400

Table 4 Reference Weber number for each experimental case

	$R_d = 1250\ \mu$m			$R_d = 950\ \mu$m			$R_d = 500\ \mu$m		
U_m, m/s	FOV 1	FOV 2	FOV 3	FOV 1	FOV 2	FOV 3	FOV 1	FOV 2	FOV 3
30	38	38	38	29	29	29	15	15	15
40	67	67	67	51	51	51	27	27	27
50	104	104	104	79	79	79	42	42	42
60	150	150	150	114	114	114	60	60	60

velocity U_m. These flowfield velocities were obtained previously by PIV on a scaled model (see Ref. [27] for details).

B. Data Analysis

Each high-speed video obtained for each run is first visualized to select three droplets. For each selected droplet, the numbers of the first frame and the last frame are recorded in an Excel sheet together with the run conditions. Then, using an in-house developed software [37], each frame is analyzed to obtain the main droplet characteristics at each time. First, the frame image is cropped to obtain a smaller region that contains only the droplet that is being analyzed. Then, the image is converted to binary image choosing the threshold that minimizes the intraclass variance of the thresholded black and white pixels. The resulting image is filtered to clean the dust and eliminate the glints. Finally, the following main droplet parameters are acquired and recorded: 1) droplet centroid position; and 2) maximum diameter, minimum diameter, and orientation of the superimposed ellipse that has the same normalized second central moments as the droplet region.

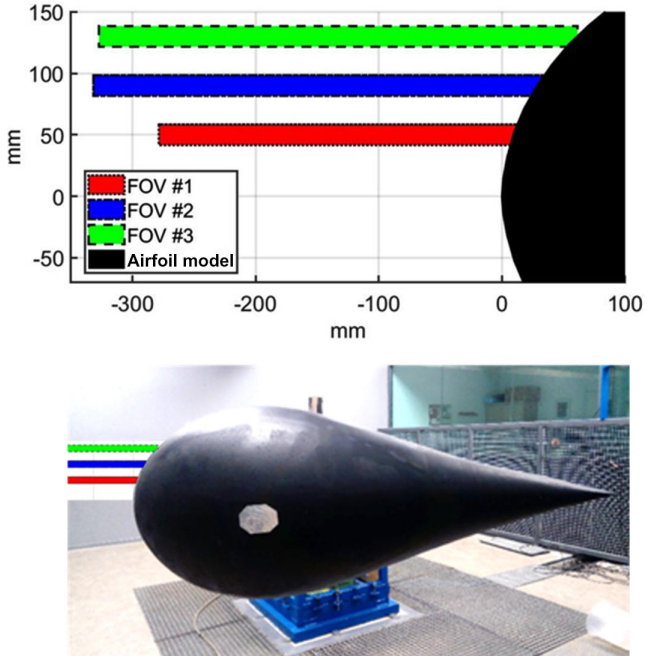

Fig. 6 Fields of view tested.

Data are then postprocessed to obtain horizontal droplet position with respect to the droplet initial position and the vertical position with respect to the stagnation line of the airfoil model, called x and y. The x droplet position vs time is fitted by a polynomial of 12th degree (see Fig. 8b). The y droplet position vs time is also fitted by a polynomial of 12th degree (see Fig. 8c). From previous fitted curves, the droplet horizontal and vertical velocities are calculated via derivation. Then, the frame where the model appears is visualized and a point in the model edge is selected manually. The curve of the model edge that passes through the point selected is superimposed to the frame for checking purposes. Because the model moves at a constant velocity (which is measured during the tests and it is, therefore, known), the position of the model at each time is calculated based on the calculation of the distance to the model at each time. Using PIV measurements previously taken from the same airfoil profile in the rotating arm facility (see Ref. [27]), the air velocity generated by the airfoil at the location of the droplet at each time is calculated.

As an example, the data analysis of an experimental case (case 32) is shown in Fig. 8. On the left (Fig. 8a), cropped images of some frames during the deformation process are displayed. In those frames, the ellipse used in the analysis is superimposed in red. Also, the air velocity is displayed as a red line whose length is proportional to the velocity magnitude. The time for each frame corresponding to each image appears on the top left of each cropped image. It could be guessed from the images that the droplet deforms as a conjunction of two half-oblate spheroids. Under this hypothesis, the volume of the droplet would be

$$(4\pi/3)(D_{\max}/2)^2(D_{\min}/2)$$

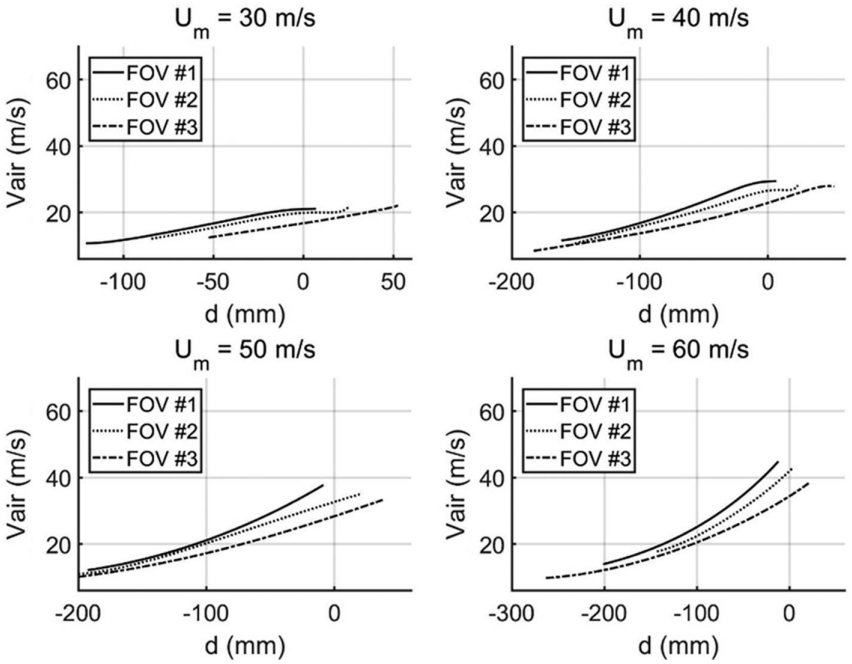

Fig. 7 Air velocity modulus versus horizontal distance to airfoil model stagnation point.

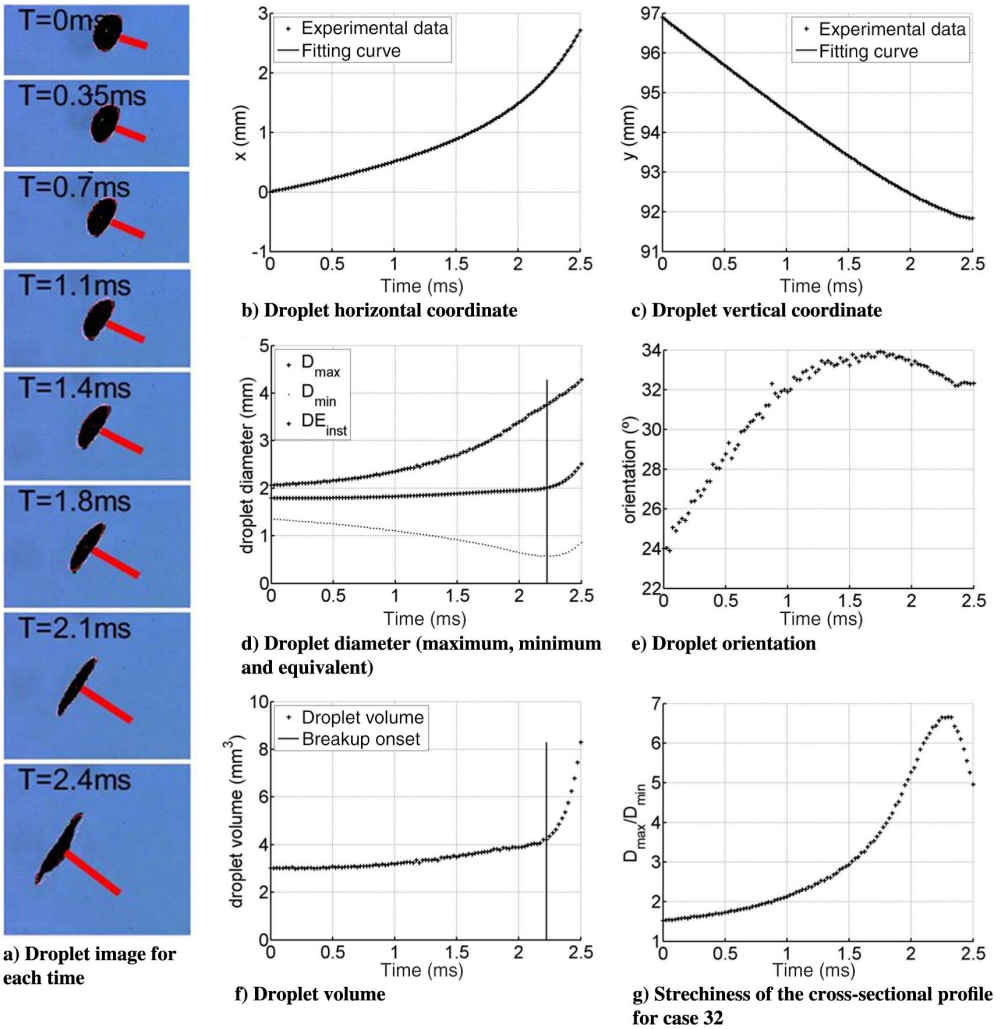

a) Droplet image for each time

b) Droplet horizontal coordinate

c) Droplet vertical coordinate

d) Droplet diameter (maximum, minimum and equivalent)

e) Droplet orientation

f) Droplet volume

g) Strechiness of the cross-sectional profile for case 32

Fig. 8 a) Droplet image for each time and b–g) data obtained in the data analysis for case 32.

As observed in Fig. 8e, the volume remains constant up to the moment at which there are global minima in the minimum diameter curve vs time. Both the maximum and minimum droplet diameters are plotted in Fig. 8d vs time. As observed, in this case, the minimum diameter curve is a convex shape and has a global minimum that can be calculated (in this case, $T = 2.2$ ms). A vertical line has been superimposed at this point. According to Refs. [24,34], this point could be considered the breakup onset definition. The equivalent diameter, defined as the one that has a sphere of the same volume, is plotted also in Fig. 8d. It can be observed that this instantaneous equivalent diameter remains constant up to the breakup onset definition within an error of 10%. Therefore, the hypothesis of droplet deformation as a conjunction of two half-spheroids seems to be valid within an error of 10%. Looking at the cropped images of the droplet, the point of the breakup onset definition corresponds to an intermediate point between the two last cropped images. It can be observed that, in the last cropped image, a front bulge has appeared and the hypothesis of two half-spheroid deformation is no longer valid. Therefore, the breakup onset definition corresponds to the point at which the droplet stops being a conjunction of two half-spheroids. Finally, the ratio of the maximum and minimum droplet diameters is shown in Fig. 8g as a measure of the stretchiness of the cross-sectional profile. It is observed that the stretchiness increases with time up to the point where global maxima appear, but this maximum occurs after the breakup onset definition. The deformation data used would be only the data analyzed up to the breakup onset definition.

IV. Results and Discussion

For cases 1–9 and 28–36, the images for different times of the droplet deformation evolution for each set of three cases with the same airfoil model velocity and same droplet size but different FOV are shown in Fig. 9 and Figs. A1–A5 in the Appendix. Figure 9 shows the cases of model velocity of 30 m/s and the biggest droplet size ($R_d = 1.25$ mm). From left to right, the FOV is increased, and therefore, droplets are in a higher region of the shoulder.

First of all, it can be observed that droplets deform as a conjunction of two half-spheroids during the deformation period. The same is observed in the other figures (Figs. A1–A5). In the previous studies of Sor et al. [33], the local figures found during the deformation period of droplets (see figs. 12–14 of Ref. [33]) differ from the conjunction of two half-spheroids. It was argued that a possible explanation for this could have been the interferences between droplets; however, it was not proved. Looking at the results presented now (where the distance between droplets has been increased respect to before notaly), it seems that, indeed, those strange local figures were due to the interferences. Additionally, it was also argued that the increase found in the error when applying the model of Sor et al. [29] was also due to these figures that depart from the assumption of oblate spheroid. Therefore, it is interesting to apply this model again now that droplets do not show the same local figures as before.

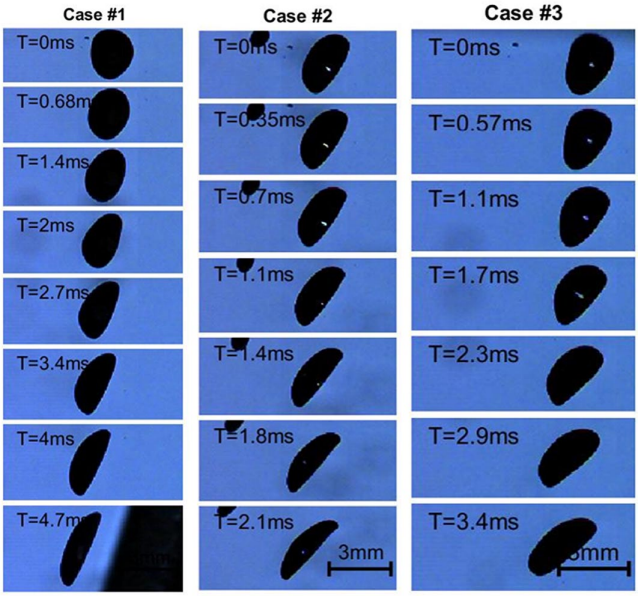

Fig. 9 Droplet deformation evolution for cases 1, 2, and 3.

The model of Sor et al. [29] was formally derived under the following assumptions:

1) The component of the incoming airflow in the x direction is much larger than in the y direction: $|V_{\text{air}\_y}| \ll |V_{\text{air}\_x}|$.

2) Droplets deform as an oblate spheroid.

3) Droplets deform only along the vertical direction that is perpendicular to the much larger horizontal slip velocity.

These hypotheses are no longer valid in the shoulder region of an airfoil: Both components of the air velocity are on the same order, droplets do not deform perpendicular to the horizontal slip velocity and also droplets deform as a conjunction of two half-spheroids. Therefore, these assumptions are modified in the present model so as to be valid in the shoulder region, with the new assumptions as follows:

1) Droplets deform as a conjunction of two half-spheroids. If the minimum half-diameters of each half spheroid are b_1 and b_2, then the total mass of the droplet would be the same as an equivalent oblate spheroid of minimum diameter $D_{\min} = b_1 + b_2$. Each value of the minimum half-diameter of each half-spheroid is not obtained from the model, but the value of the minimum diameter of the equivalent spheroid could be obtained.

2) Droplets deform only in the direction perpendicular to the slip velocity at each time. This assumption implies that droplets tilt so as to be perpendicular to the slip velocity. It can be observed from Fig. 9 that droplets tilt as the model approaches them, and that this tilting is bigger in the higher region of the shoulder.

Under these modified assumptions and the rest of the assumptions of the model of Sor et al. [29], the equations of the models are obtained [see Eqs. (1–3)]. The model consists of two dynamic equations of the droplet motion in both vertical [Eq. (2)] and horizontal [Eq. (1)] axes and another equation of the droplet deformation [Eq. (3)]. In the dynamics equations, the only forces considered are the drag force and the weight force. The drag coefficient is modeled as a sum of a stationary term, which is an interpolation between the sphere and the disk drag coefficients, and a nonstationary term. The nonstationary term depends on the variation of the slip velocity by means of a constant k. The value of this constant was assumed to be the same as the one obtained experimentally in the model of Sor et al. [29], being its value 9. For the deformation equation [Eq. (3)], the droplet is divided into two halves, and all the forces acting upon one-half are considered. The first term on the right in Eq. (3) corresponds to the viscosity term, the second to surface tension term, and the third one to the external pressure forces. The viscosity term is calculated under the assumption of pure extensional flow. The pressure force is considered to be proportional to the dynamic pressure and the droplet projected area. The proportionality coefficient C_p was found to be 0.93 in the Sor et al. model [29], and it is assumed to have the same value in the present model. For a more complete explanation of each term, the author is referred to Ref. [29]. The final equations are as follows:

$$\frac{d^2x}{dT^2} = \frac{3\rho_{\text{air}} V_s}{32\pi R_d^3 \rho_d}\left(V_{\text{air}_x} - \frac{dx}{dT}\right)\pi D_{\max}^2 \times \left(C_{D_{\text{sphere}}}^{(2R_d/D_{\max})^3} \cdot C_{D_{\text{disk}}}^{1-(2R_d/D_{\max})^3} + k\frac{2R_d}{D_{\max}^2 V_s^2}\frac{dV_s}{dT}\right) \quad (1)$$

$$\frac{d^2y}{dT^2} = -\frac{3\rho_{\text{air}} V_s}{32\pi R_d^3 \rho_d}\left(V_{\text{air}_y} - \frac{dy}{dT}\right)\pi D_{\max}^2 \times \left(C_{D_{\text{sphere}}}^{(2R_d/D_{\max})^3} \cdot C_{D_{\text{disk}}}^{1-(2R_d/D_{\max})^3} + k\frac{2R_d}{D_{\max}^2 V_s^2}\frac{dV_s}{dT}\right) + g \quad (2)$$

$$\frac{d^2D_{\max}}{dT^2} = -\frac{1024}{9}\frac{\mu_d}{D_{\max}^2}\frac{dD_{\max}}{dT} - \frac{64}{3}\frac{\sigma}{\pi R_d^3}\frac{dA_d}{dD_{\max}} + \frac{4C_P\rho_{\text{air}}}{R_d}\left(\left(V_{\text{air}_x} - \frac{dx}{dT}\right)^2 + \left(V_{\text{air}_y} - \frac{dy}{dT}\right)^2\right) \quad (3)$$

where the slip velocity is calculated as follows:

$$V_s = \sqrt{\left(V_{\text{air}_x} - \frac{dx}{dT}\right)^2 + \left(V_{\text{air}_y} - \frac{dy}{dT}\right)^2}$$

Now, it is convenient to rewrite Eqs. (1–3) in dimensionless form. To this end, the following dimensionless variables and parameters are defined as in Ref. [29]:

$$\eta = \frac{x}{R_d}, \qquad \zeta = \frac{y}{R_d}, \qquad \alpha = \frac{D_{\max}}{2R_d}, \qquad \tau = \frac{TU_m}{R_c}$$

$$\mathbb{V}_{sx} = \frac{V_{\text{air}_x} - (dx/dT)}{U_m}, \qquad \mathbb{V}_{sy} = \frac{V_{\text{air}_y} - (dy/dT)}{U_m},$$

$$\mathbb{V}_s = \frac{V_s}{U_m}, \qquad \mathbb{F}(\alpha) = \frac{2}{R_d}\frac{dA_d}{dD_{\max}}$$

where R_d is the droplet initial radius; U_m is the model velocity; and R_c is the airfoil model leading-edge radius, which, in the case of the experiments, has a value of 156 mm. Finally, the dimensionless form of Eqs. (1–3) follows:

$$\frac{d^2\eta}{d\tau^2} = \Pi_1\alpha^2\mathbb{V}_s\mathbb{V}_{sx}\left[\left(C_{D_{\text{sphere}}}^{(1/\alpha)^3}\cdot C_{D_{\text{disk}}}^{1-(1/\alpha)^3}\right) + \left(\Pi_2\frac{1}{\alpha^2\mathbb{V}_s^2}\frac{d\mathbb{V}_s}{d\tau}\right)\right] \quad (4)$$

$$\frac{d^2\zeta}{d\tau^2} = -\Pi_1\alpha^2\mathbb{V}_s\mathbb{V}_{sy}\left[\left(C_{D_{\text{sphere}}}^{(1/\alpha)^3}\cdot C_{D_{\text{disk}}}^{1-(1/\alpha)^3}\right) + \left(\Pi_2\frac{1}{\alpha^2\mathbb{V}_s^2}\frac{d\mathbb{V}_s}{d\tau}\right)\right] + \Pi_3 \quad (5)$$

$$\frac{d^2\alpha}{d\tau^2} = -\Pi_4\mathbb{F}(\alpha) - \Pi_5\frac{1}{\alpha^2}\frac{d\alpha}{d\tau} + \frac{16}{3}\Pi_1 C_P\mathbb{V}_s^2 \quad (6)$$

where Π_1, Π_2, Π_3, Π_4, and Π_5 are the following dimensionless parameters:

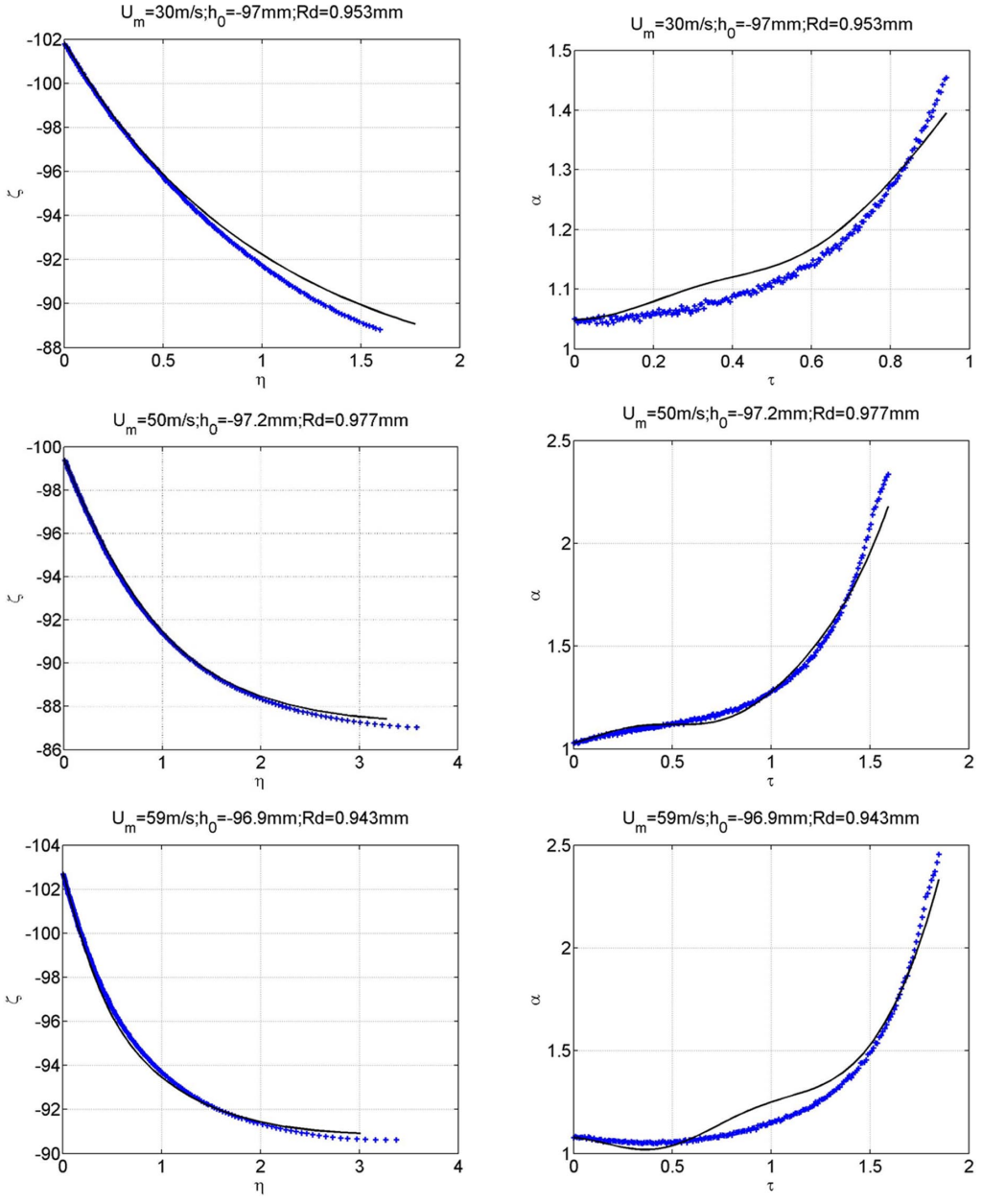

Fig. 10 Comparison between the model solution (line) and experimental data (asterisk markers).

$$\Pi_1 = \left[\frac{3}{8}\frac{\rho_{\text{air}}}{\rho_d}\left(\frac{R_c}{R_d}\right)^2\right], \qquad \Pi_2 = \frac{kR_d}{R_c}, \qquad \Pi_3 = \frac{gR_c}{U_m^2}\left(\frac{R_c}{R_d}\right),$$

$$\Pi_4 = \frac{16}{3\pi}\frac{\sigma}{\rho_d}\left(\frac{R_c}{U_m R_d}\right)^2\frac{1}{R_d}, \qquad \Pi_5 = \frac{256}{9Re}\frac{\mu_d}{\mu_{\text{air}}}\frac{\rho_{\text{air}}}{\rho_d}\frac{R_c}{R_d}$$

Equations (4–6) have been integrating using an implicit scheme of MATLAB (ode15i) and using as initial conditions those of the experiments. Results of the integration of the model vs the experimental data are shown in Figs. 10–13 for three subsets of the tested cases. Case 23 has been chosen as the reference case, and then each parameter has been variated leading to the following three subsets of cases:

1) Subset 1 (cases 5, 23, and 32): The model velocity is variated from 30 to 60 m/s.

2) Subset 2 (cases 26, 23, and 20): The droplet radius has been variated from 0.5 to 1.25 mm.

3) Subset 3 (cases 22, 23, and 24): The FOV height with respect to the stagnation line of the airfoil is variated from 50 to 130 mm.

Figure 10 shows the results of the integration of the trajectory (on the left) and the deformation (on the right) compared with the experimental data for cases 5 (on the top), 23 (in the middle), and 32 (on the bottom). It can be observed that, in these cases, the model predicts the experimental results with the same level of accuracy regardless of the model velocity for each case. In an analogous figure, Fig. 11 shows the results for cases 26 (top), 23 (in the middle), and 20 (bottom). In this case, the droplet radius is variated. It can be observed that the model works with a reasonable level of accuracy for the three cases. However, in this case, the error seems to increase with the droplet radius. Bigger droplets have larger response times, which means that it takes more time for them to react to external forces. One of the assumptions of the model was that the droplets deform only perpendicular to the slip velocity, which means that the droplets should tilt so as to be perpendicular to the slip velocity, which changes its direction in the shoulder region. The tilting should be rapid enough so as to follow the change in direction of the slip velocity, and for bigger droplets, this is more difficult to be attained. The increase in the error with the droplet radius could be due to the

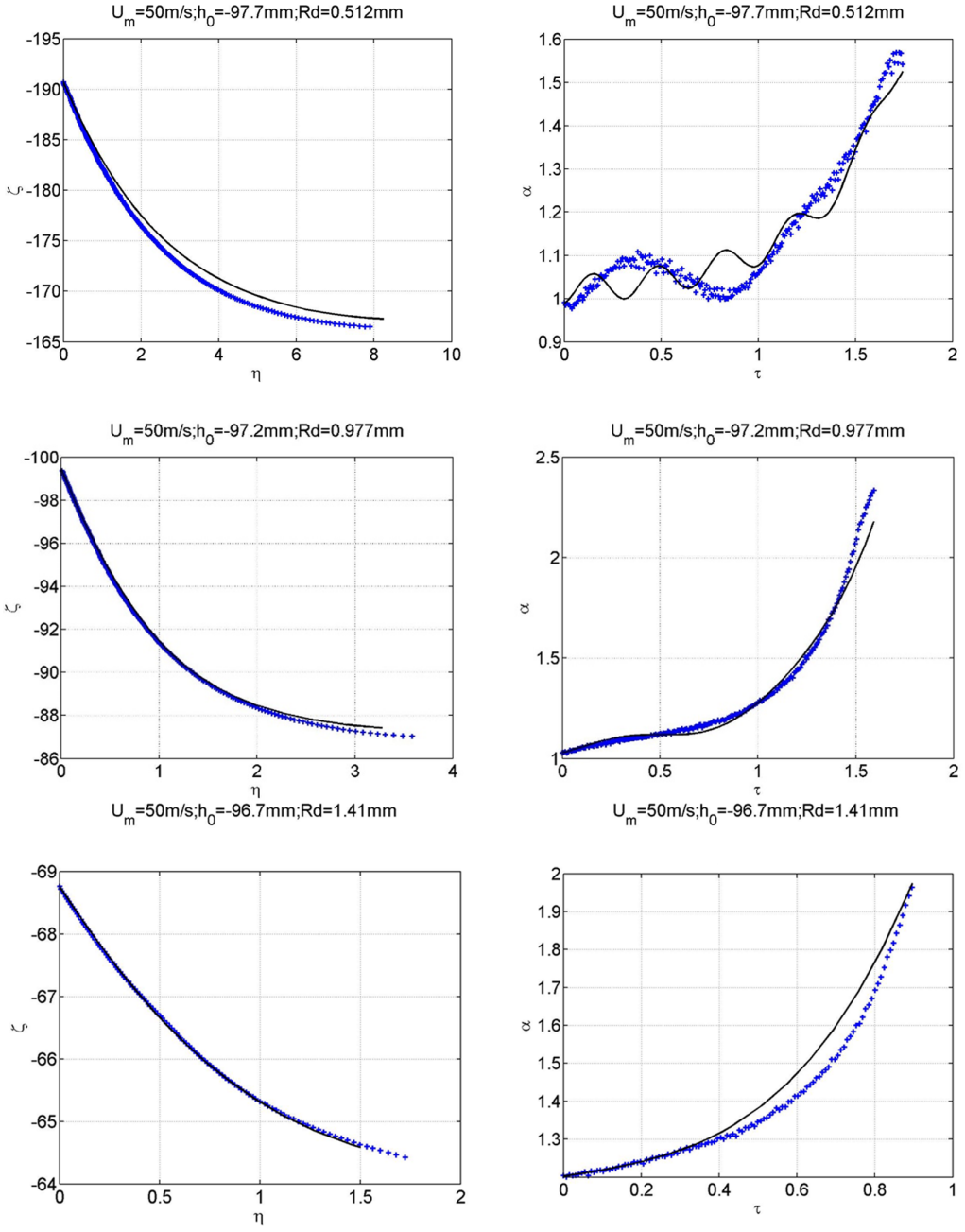

Fig. 11 Comparison between the model solution (line) and experimental data (asterisk markers).

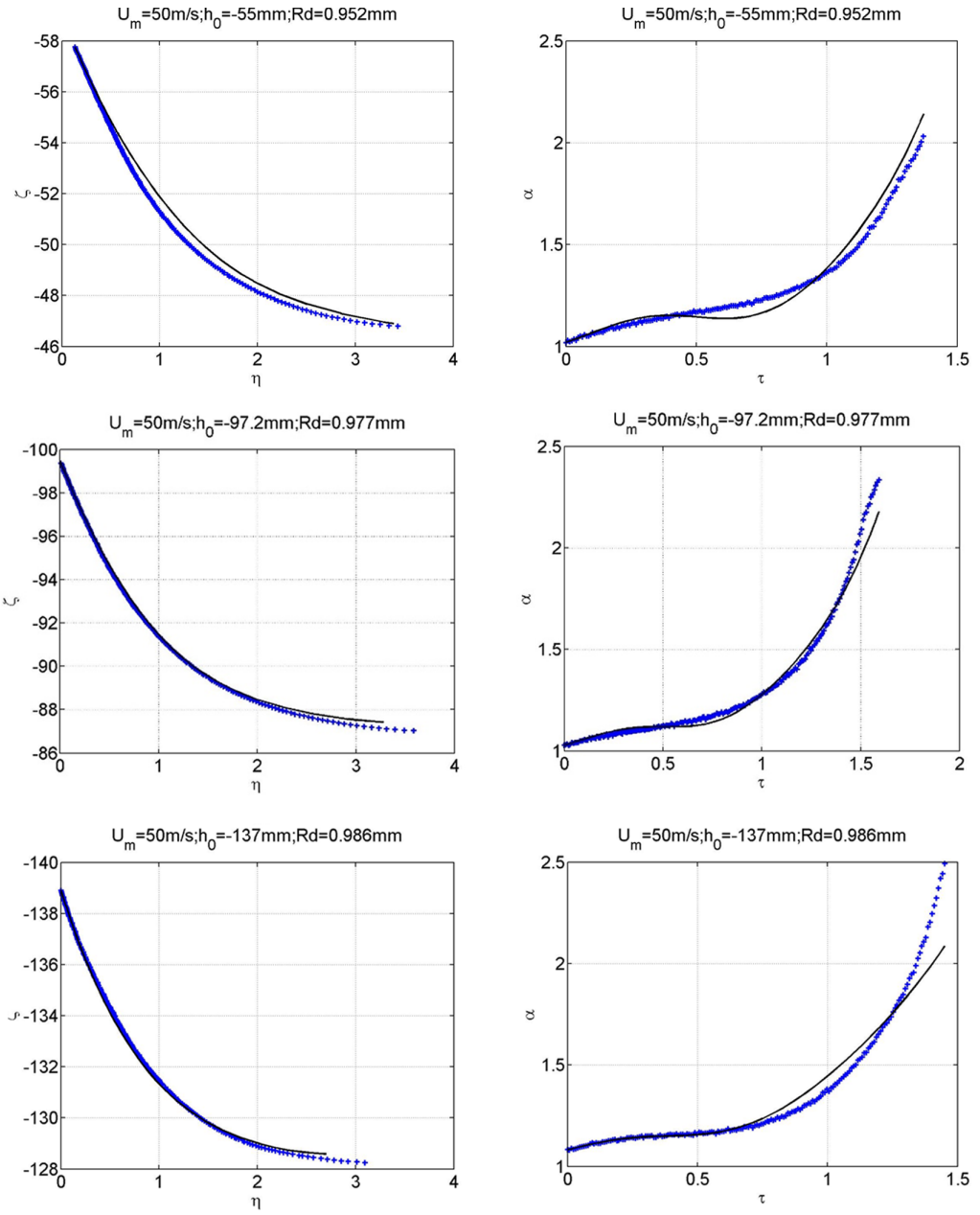

Fig. 12 Comparison between the model solution (line) and experimental data (asterisk markers).

larger response time of these droplets as it will be discussed later. On the other hand, for case 26, which corresponds to smaller droplets, the experimental deformation ratio exhibits a periodic behavior. The reason for this periodic behavior remains in the initial oscillations of the droplet. Figure 13 has been built to show these oscillations. On the left, a sequence of the experimental images is shown, whereas on the right, the maximum, minimum, and equivalent diameters; the droplet volume; and the droplet orientation are displayed. Because of its generation, in this case, a three-dimensional oscillation is observed in the droplet behavior, and therefore, the calculated droplet volume would also exhibit a periodic oscillation. This does not happen in the rest of the cases (see Fig. 8).

Finally, Fig. 12 is an analogous figure to Figs. 11 and 10, but for cases 22, 23, and 24. In this subset, the FOV height is variated, being FOV 1 (case 22) the one nearest to the stagnation line of the airfoil and FOV 3 (case 24) the highest one. Again, the results of the model integrations seem to predict adequately the experimental data, being in this subset the maximum discrepancy found in the highest FOV (FOV 3). This could be explained as before taken into account that, in the highest FOV, the angle of the slip velocity changes more rapidly compared with the other FOV.

It can be observed in Figs. 10–12 that the model predicts with a very good agreement with the experimental data. However, it is important to quantify these differences to be able to compare with the previous results in the shoulder region [33] and the previous results in the stagnation line [29]. Although only the results of three subsets have been shown, the model has been integrated for all the experimental cases obtained during the tests, summarized in Table 2. The discrepancies have been calculated for both the trajectory and the deformation defining the error for the trajectory and the error for the deformation for each experimental test data as follows:

$$\text{Error}\,\alpha(\%) = 100 \cdot \frac{1}{n}\sum_{i=1}^{n}\frac{|\alpha_i - \alpha_{\text{exp}}|}{|\alpha_{\text{exp}}|};$$

$$\text{Error}_{\text{trajectory}}(\%) = \sqrt{(\text{Error}\,\eta)^2 + (\text{Error}\,\zeta)^2}$$

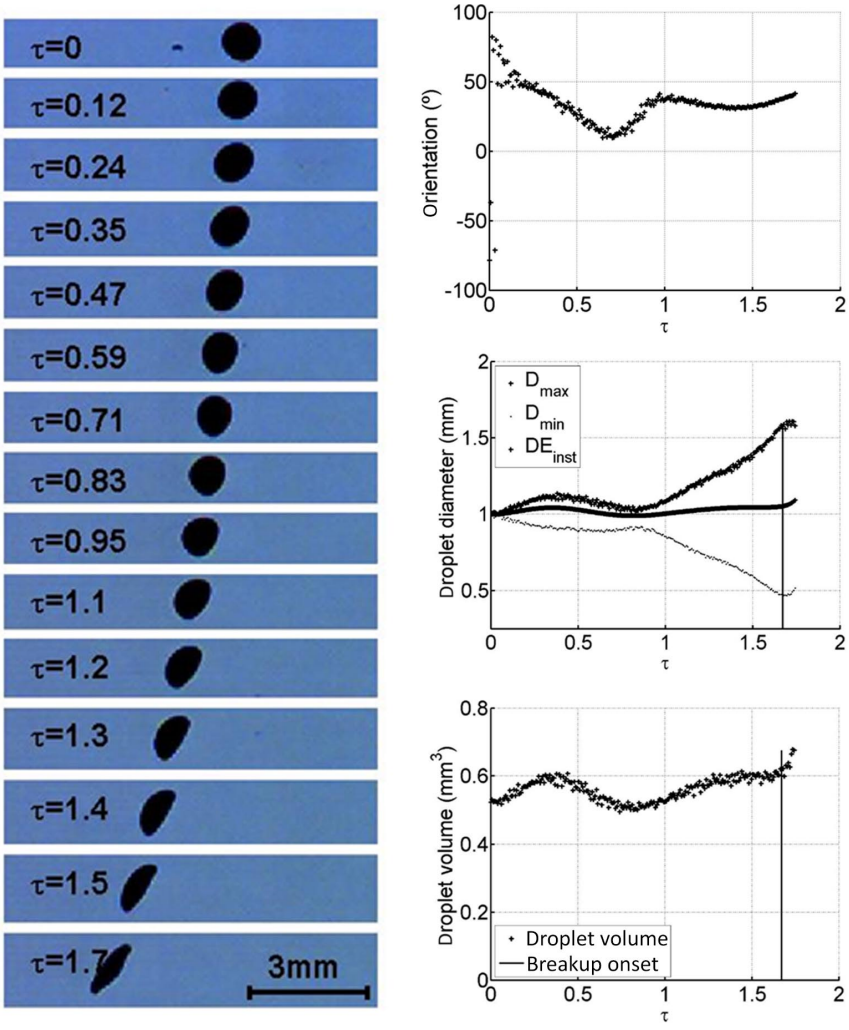

Fig. 13 Experimental data of case 26.

where

$$\text{Error}\,\eta(\%) = 100 \cdot \frac{1}{n}\sum_{i=1}^{n}\frac{|\eta_i - \eta_{\text{exp}}|}{\max(|\eta_{\text{exp}}|)};$$

$$\text{Error}\,\zeta(\%) = 100 \cdot \frac{1}{n}\sum_{i=1}^{n}\frac{|\zeta_i - \zeta_{\text{exp}}|}{\max(|\zeta_{\text{exp}}|)}$$

Figure 14 shows the error for the trajectory and the deformation calculated for each experimental case. Additionally, for each of the cases of the matrix of Table 2, the mean and the maximum of the errors are calculated. Table 5 shows the results obtained. First, a clear tendency of the increase of the error with the droplet radius can be observed in Fig. 14, being the maximum error for droplets of 0.5 mm of radius on the order of 3% for the trajectory and 8% for the deformation. The maximum errors for the bigger droplets are on the order of 8% for the trajectory and 15% for the deformation, which are still reasonable errors.

Now, looking in more detail (Table 5), it can be observed that the mean error for the deformation is always less than 6% except for three cases that correspond to FOV 3, which is the highest FOV height and

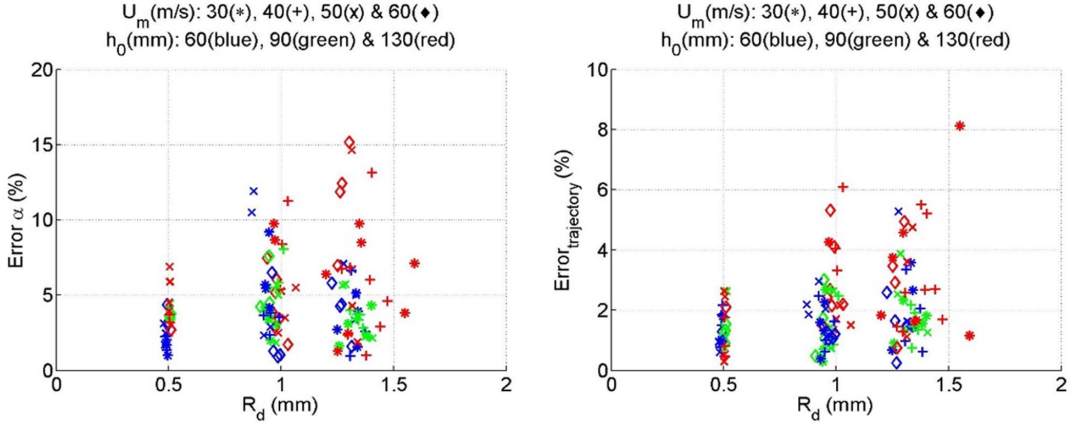

Fig. 14 Droplet trajectory error (left) and droplet deformation error (right) vs droplet radius.

Table 5 Mean error for cases of Table 2

Case key	Number of cases analyzed	U_m, m/s	R_d, mm	h_0, mm	Mean error η, %	Maximum error η, %	Mean error α, %	Maximum error α, %
1	7	30	1.25	60	2.1	3.6	3.4	6.6
2	8	30	1.25	95	1.5	2.3	3.2	4.0
3	8	30	1.25	130	2.3	4.6	5.5	9.7
4	8	30	1	60	1.4	2.5	4.7	9.2
5	8	30	1	95	1.4	2.7	4.7	8.1
6	5	30	1	130	3.8	6.1	8.7	11.3
7	9	30	0.5	60	1.3	2.2	1.7	2.3
9	4	30	0.5	130	0.9	1.7	3.3	3.7
10	7	40	1.25	60	2.3	5.3	4.6	7.1
11	9	40	1.25	95	1.9	3.9	3.9	5.7
12	6	40	1.25	130	2.5	4.8	6.1	14.6
13	7	40	1	60	1.8	3.0	4.4	11.9
14	4	40	1	95	1.8	2.7	5.6	8.1
15	7	40	1	130	2.9	6.1	6.0	11.3
16	7	40	0.5	60	1.2	2.2	2.2	3.1
17	3	40	0.5	95	1.4	2.6	4.0	4.4
18	8	40	0.5	130	1.2	2.6	4.3	6.9
19	9	50	1.25	60	1.8	5.3	4.7	7.1
20	3	50	1.25	95	2.7	3.9	4.6	5.7
21	7	50	1.25	130	3.1	4.9	9.6	15.2
22	7	50	1	60	1.6	3.0	3.8	11.9
23	8	50	1	95	1.6	3.0	4.2	7.6
24	11	50	1	130	2.5	5.3	4.3	7.5
25	6	50	0.5	60	0.9	1.3	3.0	4.3
26	7	50	0.5	95	1.3	2.6	3.8	4.4
27	5	50	0.5	130	1.6	2.6	4.8	6.9
28	5	60	1.25	60	1.2	2.6	4.1	5.8
30	4	60	1.25	130	3.0	4.9	11.6	15.2
31	4	60	1	60	1.1	1.3	2.4	6.5
32	8	60	1	95	1.6	3.0	4.2	7.6
33	7	60	1	130	2.9	5.3	4.3	7.5
34	3	60	0.5	60	1.1	1.3	3.5	4.3
35	4	60	0.5	95	1.2	1.5	3.6	3.8
36	1	60	0.5	130	2.1	2.1	2.7	2.7

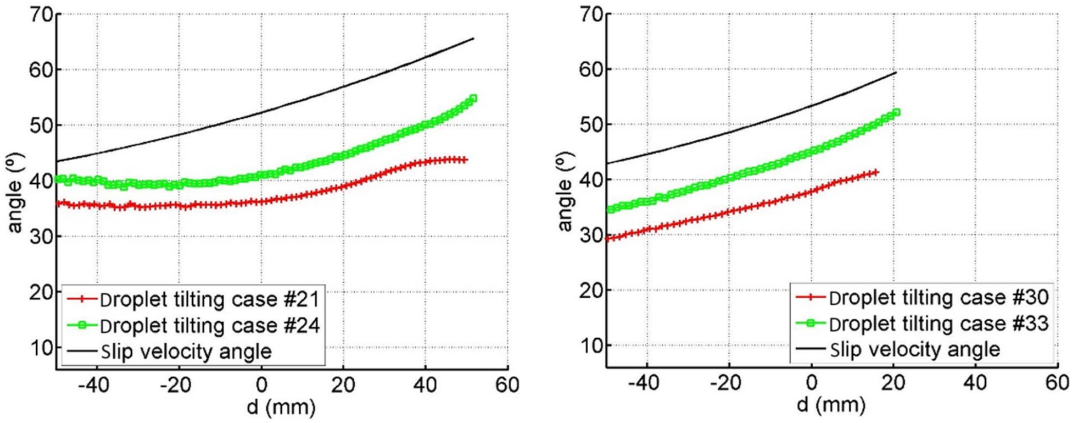

Fig. 15 Tilting and velocity angles versus horizontal distance to airfoil model stagnation point.

thus the biggest changes in the air direction. In particular, cases 21 and 30 are the worst cases, where the errors are up to 12%. These two cases correspond not only to the highest FOV, but also to the bigger droplet size. According to the previous reasoning, droplets of bigger sizes have bigger response times, which prevent them from tilting so as to be perpendicular to the slip velocity. Indeed, this is the case. In Fig. 15, the angles of the slip velocity (with respect to the horizontal) and the angle of the tilting (with respect to the vertical) are compared for cases 21 and 24 (on the left), and cases 30 and 33 (on the right). Cases 21 and 30 correspond to droplet radius of 1.25 mm, whereas cases 24 and 33 correspond to droplet radius of 0.95 mm. In any case, the average error found for droplets of radius below 1 mm was found to be on the 3% for the trajectory and 6% for the deformation. Further studies could be done in the future for bigger droplets, using the experimental data here, to modify the model to account for the tilting observed in the deformation images.

On the other hand, the mean error for the trajectory is on the order of 3%, which is similar to the discrepancy found in the stagnation line of the airfoil on the order of 3.6% [29] and is half the order of the previous results in the shoulder region [33] on the order of 6.4%. Therefore, it could be confirmed that the increase in the error found in previous results [33] was indeed due to the interference effects, as suspected.

V. Conclusions

New experiments have been conducted on droplet deformation and movement in the shoulder region of an incoming airfoil at the rotating arm installation at INTA. Three different regions of the shoulder at

different heights, three droplet sizes, and four model velocities have been tested. Droplets deform as a conjunction of two half-spheroids. Additionally, there is an appreciable tilting in this region that increases with the height of the region. The deformation figures found in the previous results in the shoulder region [33] that departs from the assumption of an oblate spheroid deformation have not been found in the experimental results of the present study, where the distance between droplets has been increased. Therefore, it can be concluded that the deformation figures previously found were due to the interferences between droplets.

The trajectory model of Sor et al. [29], formally derived in the stagnation line of an airfoil, has now been formally derived for the shoulder region of the airfoil, assuming that droplets deform perpendicular to the slip velocity, which means that droplets tilt so as to be perpendicular to the slip velocity. The new formulation for the shoulder region of the airfoil has been validated for the range of parameters tested, being the discrepancies found on the order of 3% for the trajectory and 6% for the deformation in the majority of the cases. Only there is a bigger discrepancy in the deformation (on the order of 12%) for the droplets of 1.25 mm in the highest region tested, which was explained due to the larger response times of the droplets and the more rapid change in the slip velocity direction.

Appendix: Images of Droplet Deformation Evolution

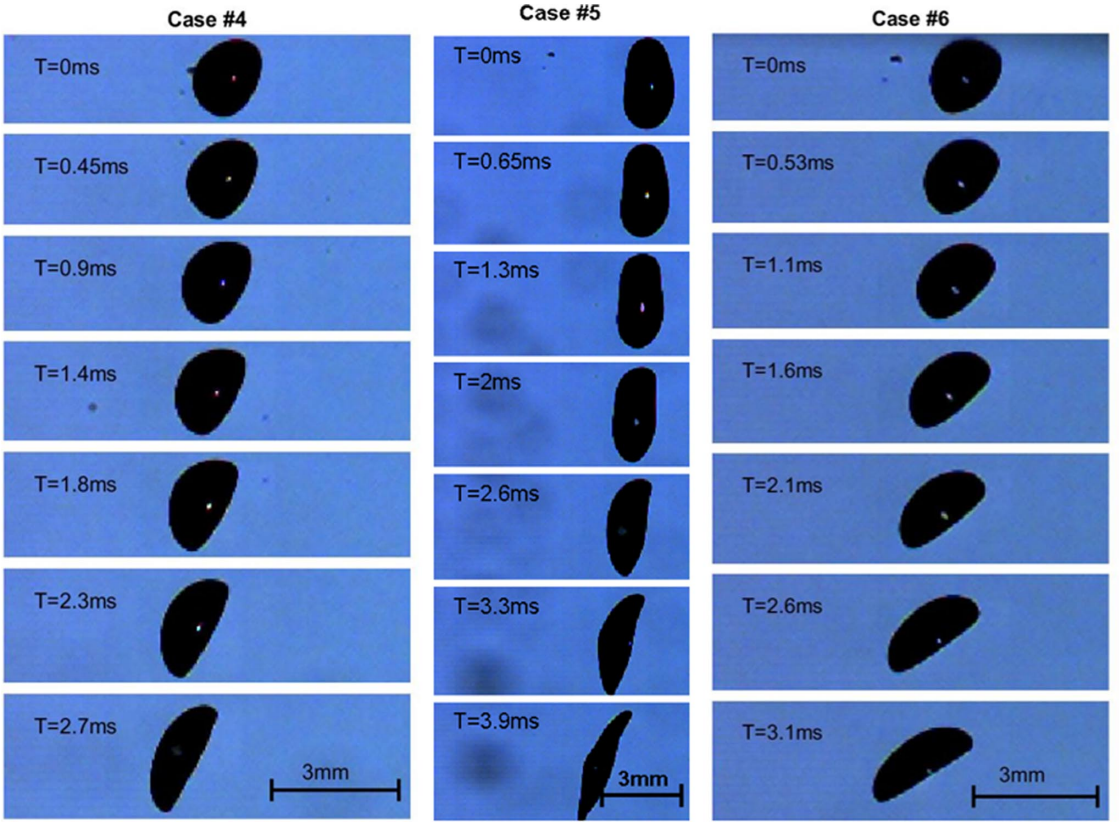

Fig. A1 Droplet deformation evolution for cases 4, 5, and 6, which correspond to an airfoil model velocity of 30 m/s; a droplet radius of 0.950 mm; and FOV 1, 2, and 3, respectively.

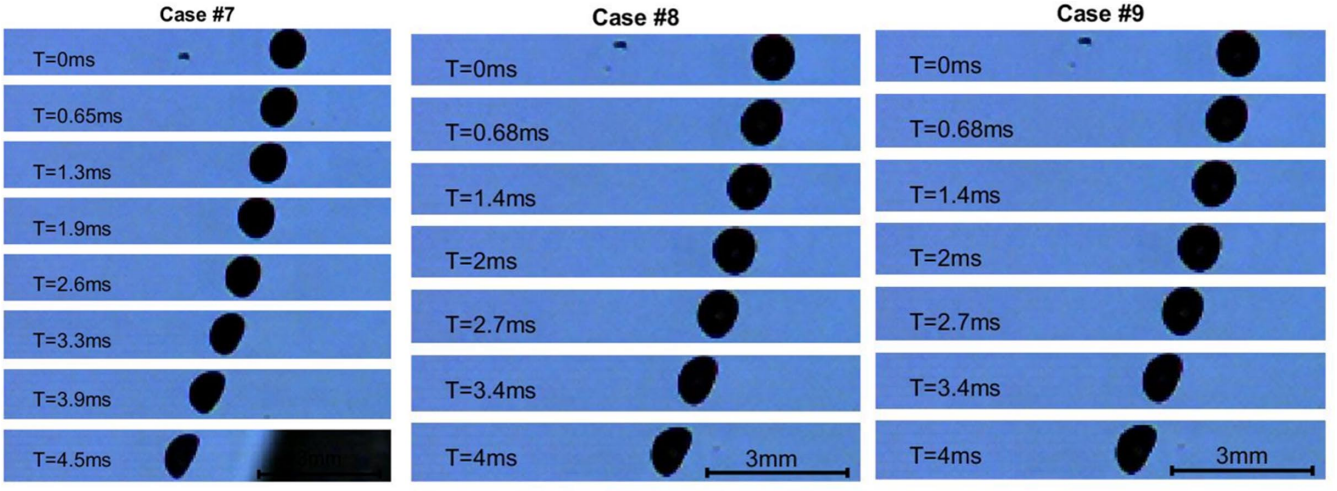

Fig. A2 Droplet deformation evolution for cases 7, 8, and 9, which correspond to an airfoil model velocity of 30 m/s; a droplet radius of 0.5 mm; and FOV 1, 2, and 3, respectively.

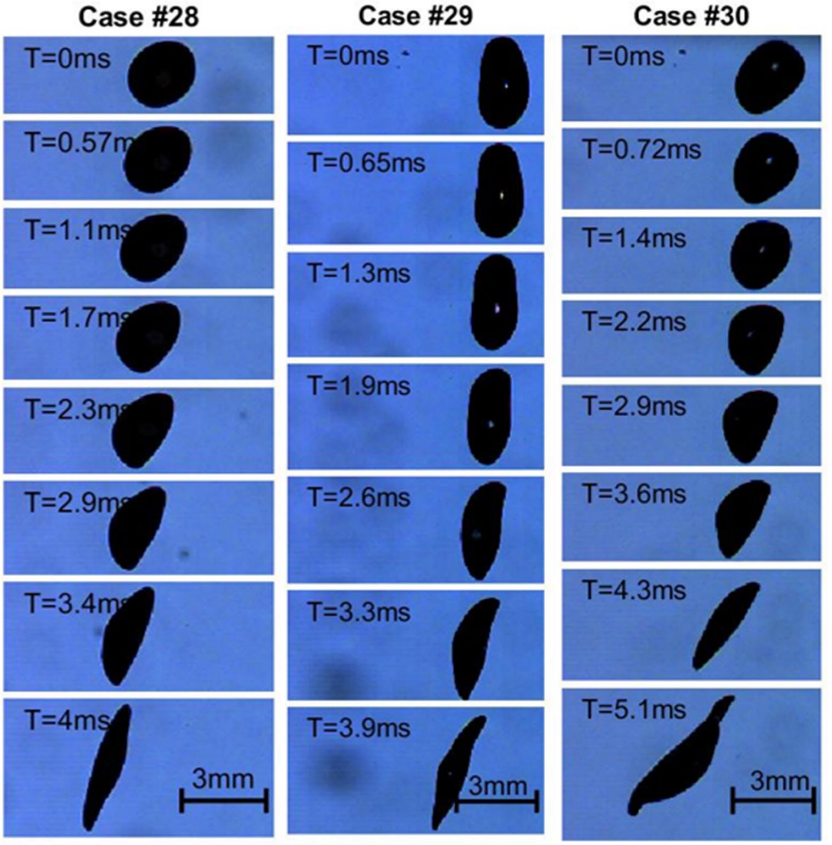

Fig. A3 Droplet deformation evolution for cases 28, 29, and 30, which correspond to an airfoil model velocity of 60 m/s; a droplet radius of 1.25 mm; and FOV 1, 2, and 3, respectively.

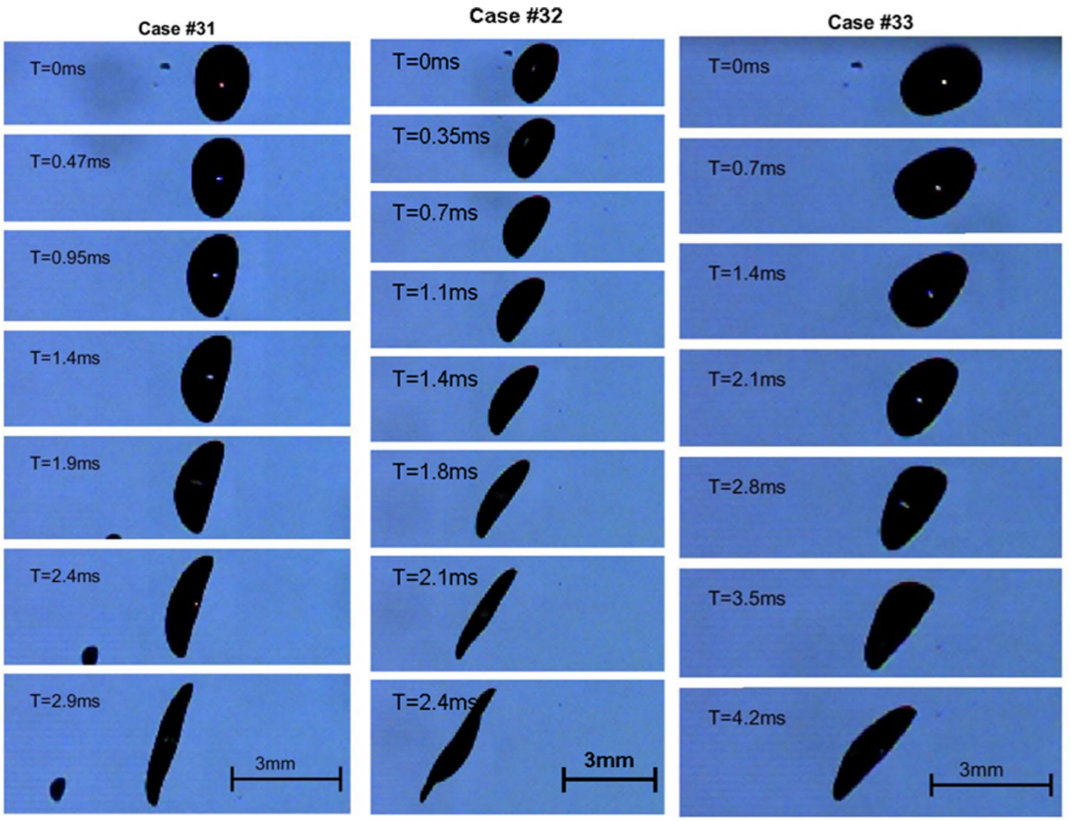

Fig. A4 Droplet deformation evolution for cases 31, 32, and 33, which correspond to an airfoil model velocity of 60 m/s; a droplet radius of 0.950 mm; and FOV 1, 2, and 3, respectively.

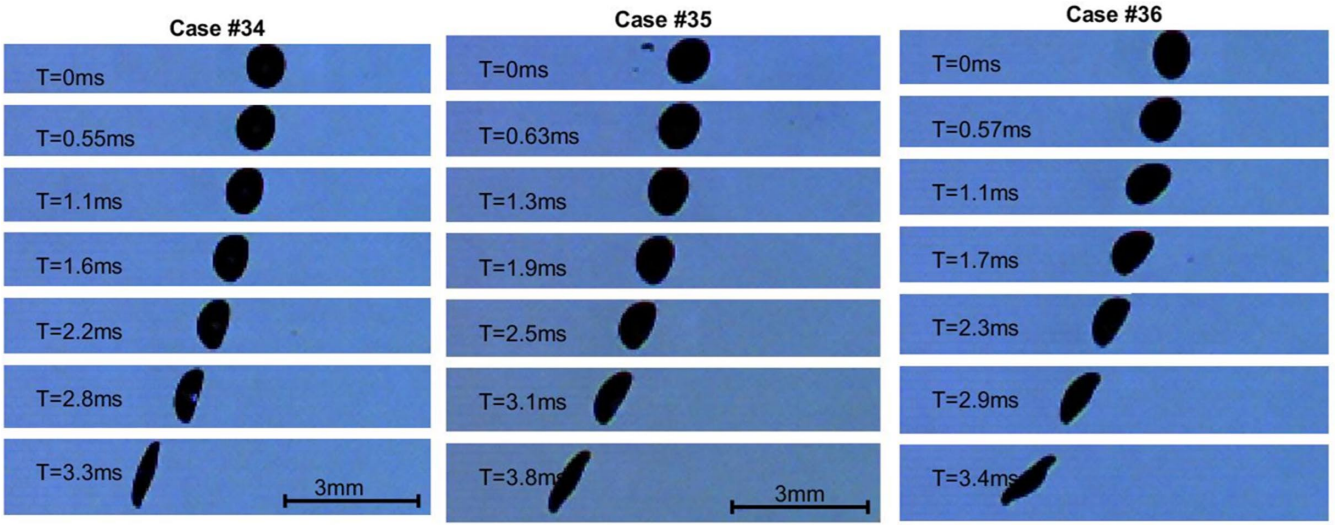

Fig. A5 Droplet deformation evolution for cases 34, 35, and 36, which correspond to an airfoil model velocity of 60 m/s; a droplet radius of 0.5 mm; and FOV 1, 2, and 3, respectively.

Acknowledgments

This investigation has been funded by the Ministry of Economy, Industry and Competitiveness of Spain as part of the project DFLOW DPI2016-75296-P. This has also been funded by the Instituto Nacional de Técnica Aeroespacial, under the project "Termofluidodinámica." The authors want to thank Mar Urdiales for her valuable help during the processing of the data.

References

[1] Özgen, S., Ugur, N., Görgülü, I., and Tatar, V., "Ice Accretion Simulations of Airfoils," *Progress in Flight Physics*, Vol. 9, June 2017, pp. 107–126. https://doi.org/10.1051/eucass/2016090107

[2] Qin, F., Bai, J., and Li, X., "Supercooled Large Droplet Impingement Simulation of 3-Element Airfoils," *2017 8th International Conference on Mechanical and Intelligent Manufacturing Technologies (ICMIMT)*, IEEE, New York, pp. 225–229. https://doi.org/10.1109/ICMIMT.2017.7917469

[3] Honsek, R., Habashi, W. G., and Aubé, M. S., "Eulerian Modeling of In-Flight Icing due to Supercooled Large Droplets," *Journal of Aircraft*, Vol. 45, No. 4, 2008, pp. 1290–1296. https://doi.org/10.2514/1.34541

[4] Iuliano, E., Mingione, G., Petrosino, F., and Hervy, F., "Eulerian Modeling of Large Droplet Physics Toward Realistic Aircraft Icing Simulation," *Journal of Aircraft*, Vol. 48, No. 5, 2011, pp. 1621–1632. https://doi.org/10.2514/1.C031326

[5] Blake, J., Thompson, D., Raps, D., and Strobl, T., "Simulating the Freezing of Supercooled Water Droplets Impacting a Cooled Substrate," *AIAA Journal*, Vol. 53, No. 7, 2015, pp. 1725–1739. https://doi.org/10.2514/1.J053391

[6] Wang, C., Chang, S., and Wu, H., "Lagrangian Approach for Simulating Supercooled Large Droplets' Impingement Effect," *Journal of Aircraft*, Vol. 52, No. 2, 2015, pp. 524–537. https://doi.org/10.2514/1.C032765

[7] Trontin, P., and Villedieu, P., "Revisited Model for Supercooled Large Droplet Impact onto a Solid Surface," *Journal of Aircraft*, Vol. 54, No. 3, 2017, pp. 1189–1204. https://doi.org/10.2514/1.C034092

[8] Reehorst, A., Chung, J., Potapczuk, M., and Choo, Y., "Study of Icing Effects on Performance and Controllability of an Accident Aircraft," *Journal of Aircraft*, Vol. 37, No. 2, 2000, pp. 253–259. https://doi.org/10.2514/2.2588

[9] Baars, W. J., Stearman, R. O., and Tinney, C. E., "A Review on the Impact of Icing on Aircraft Stability and Control," *Journal of Aeroelasticity and Structural Dynamics*, Vol. 2, No. 1, 2010, pp. 35–52.

[10] Caliskan, F., and Hajiyev, C., "A Review of In-Flight Detection and Identification of Aircraft Icing and Reconfigurable Control," *Progress in Aerospace Sciences*, Vol. 60, July 2013, pp. 12–34. https://doi.org/10.1016/j.paerosci.2012.11.001

[11] Hospers, J., and Hoeijmakers, H., "Numerical Simulation of SLD Ice Accretions," SAE International Soc. of Automotive Engineers TP 2011-38-0071, 2011, https://doi.org/10.4271/2011-38-0071

[12] Laschka, B., and Jesse, R. E., "Ice Accretion and Its Effects on Aerodynamics of Unprotected Aircraft Components," Tech. Rept. 15, AGARD, Advisory Rept. 127, Nov. 1978.

[13] Tan, S. C., "Effects of Large Droplet Dynamics on Airfoil Impingement Characteristics," AIAA Paper 2005-0074, Jan. 2005.

[14] Aalburg, C., Leer, B. V., and Faeth, G. M., "Deformation and Drag Properties of Round Drops Subjected to Shock-Wave Disturbances," *AIAA Journal*, Vol. 41, No. 12, 2003, pp. 2371–2378. https://doi.org/10.2514/2.6862

[15] Mashayek, A., and Ashgriz, N., "Model for Deformation of Drops and Liquid Jets in Gaseous Crossflows," *AIAA Journal*, Vol. 47, No. 2, 2009, pp. 303–313. https://doi.org/10.2514/1.36148

[16] O'Rourke, P. J., and Amsden, A. A., "The TAB Method for Numerical Calculation of Spray Droplet Breakup," SAE International Soc. of Automotive Engineers TR-872089, 1987.

[17] Wierzba, A., "Deformation and Breakup of Liquid Drops in a Gas Stream," *Experiments in Fluids*, Vol. 9, Nos. 1–2, 1990, pp. 59–64. https://doi.org/10.1007/BF00575336

[18] Alesekyenko, S., Sinapius, M., Schulz, M., and Prykhodko, O., "Interaction of Supercooled Large Droplet with Aerodynamic Profile," SAE International Soc. of Automotive Engineers TP 2015-01-2118, 2015, https://doi.org/10.4271/2015-01-2118

[19] Shimura, M., and Yamamoto, M., "Comparative Investigation on Effect of Droplet Deformation Model on SLD Icing," SAE International Soc. of Automotive Engineers TP 2015-01-2117, 2015, https://doi.org/10.4271/2015-01-2117.

[20] Shao, C., Luo, K., and Fan, J., "Detailed Numerical Simulation of Unsteady Drag Coefficient of Deformable Droplet," *Chemical Engineering Journal*, Vol. 308, Jan. 2017, pp. 619–631. https://doi.org/10.1016/j.cej.2016.09.062

[21] Qu, Q., Ma, P., Liu, P., Li, S., and Agarwal, R. K., "Numerical Study of Transient Deformation and Drag Characteristics of a Decelerating Droplet," *AIAA Journal*, Vol. 54, No. 2, 2016, pp. 490–505. https://doi.org/10.2514/1.J054286

[22] Guan, B., Liu, Y., Wen, C. Y., and Shen, H., "Numerical Study on Liquid Droplet Internal Flow Under Shock Impact," *AIAA Journal*, Vol. 56, No. 9, 2018, pp. 3382–3387. https://doi.org/10.2514/1.J057134

[23] Meng, J. C., and Colonius, C., "Numerical Simulation of the Aerobreakup of a Water Droplet," *Journal of Fluid Mechanics*, Vol. 835, Jan. 2018, pp. 1108–1135. https://doi.org/10.1017/jfm.2017.804

[24] Vargas, M., and Feo, A., "Deformation and Breakup of Water Droplets Near an Airfoil Leading Edge," *Journal of Aircraft*, Vol. 48, No. 5, 2011, pp. 1749–1765. https://doi.org/10.2514/1.C031363

[25] Vargas, M., Sor, S., and Garcia Magariño, A., "Mechanism of Water Droplet Breakup Near the Leading Edge of an Airfoil," AIAA Paper 2012-3129, June 2012.

[26] Vargas, M., Sor, S., and Garcia Magariño, A., "Drag Coefficient of Water Droplets Approaching the Leading Edge of an Airfoil," AIAA Paper 2013-3054, June 2013.

[27] Garcia-Magariño, A., Sor, S., and Velazquez, A., "Experimental Characterization of Water Droplet Deformation and Breakup in the Vicinity of a Moving Airfoil," *Aerospace Science and Technology*, Vol. 45, Sept. 2015, pp. 490–500. https://doi.org/10.1016/j.ast.2015.06.025

[28] Sor, S., and Garcia-Magariño, A., "Modeling of Droplet Deformation Near the Leading Edge of an Airfoil," *Journal of Aircraft*, Vol. 52, No. 6, 2015, pp. 1838–1846. https://doi.org/10.2514/1.C033086

[29] Sor, S., Garcia-Magariño, A., and Velazquez, A., "Model to Predict Water Droplet Trajectories in the Flow Past an Airfoil," *Aerospace Science and Technology*, Vol. 58, Nov. 2016, pp. 26–35. https://doi.org/10.1016/j.ast.2016.07.015

[30] Garcia-Magariño, A., "Water Droplet Deformation and Breakup in the Vicinity of the Leading Edge of an Incoming Airfoil," Doctoral Thesis, Universidad Politécnica de Madrid, Madrid, 2016.

[31] Sor, S., "Theoretical Model for Droplet Deformation and Trajectory in Continuously Accelerating Flows," Doctoral Thesis, Universidad Politécnica de Madrid, Madrid, 2017.

[32] Veras-Alba, B., Palacios, J., Vargas, M., Ruggeri, C., and Barkus, T. P., "Experimental Investigation of Supercooled Water Droplet Breakup Near Leading Edge of Airfoil," *Journal of Aircraft*, Vol. 55, No. 5, 2018, pp. 1970–1984. https://doi.org/10.2514/1.C034714

[33] Sor, S., Garcia-Magariño, A., and Velazquez, A., "Rotating Arm-Based Experimental Study on Droplet Behavior in the Shoulder Region of an Aircraft Aerodynamic Surface," *International Journal of Aerospace Engineering*, Vol. 2017, Oct. 2017, Article 8390905. https://doi.org/10.1155/2017/8390905

[34] Garcia-Magariño, A., Sor, S., and Velazquez, A., "Droplet Breakup Criterion in Airfoils Leading Edge Vicinity," *Journal of Aircraft*, Vol. 55, No. 5, 2018, pp. 1867–1876. https://doi.org/10.2514/1.C034631

[35] Garcia-Magariño, A., Sor, S., and Velazquez, A., "Data Reduction Method for Droplet Deformation Experiments Based on High Order Singular Value Decomposition," *Experimental Thermal and Fluid Science*, Vol. 79, Dec. 2016, pp. 13–24. https://doi.org/10.1016/j.expthermflusci.2016.06.017

[36] Cober, S. G., and Isaac, G. A., "Characterization of Aircraft Icing Environments with Supercooled Large Drops for Application to Commercial Aircraft Certification," *Journal of Applied Meteorology and Climatology*, Vol. 51, No. 2, Feb. 2012, pp. 265–284. https://doi.org/10.1175/JAMC-D-11-022.1

[37] Sor, S., García-Magariño, A., and Morote, J., "Experimental Determination and Data Processing of Trajectories, Deformation and Breakup of Water Droplets Impinging on Airfoils," *Conference on Modelling Fluid Flow 2012*, edited by J. Vad, Vol. 1, Budapest Univ. of Technology and Economics, Budapest, 2012, pp. 192–198.

J. Floryan
Associate Editor